ILASS Europe 2023, 32nd Conference on Liquid Atomization & Spray Systems, 4-7 Sept 2023, Napoli, Italy

Spray-wall Interactions: a Study of Impinging Sprays on Transient Thermal Loading and Fuel Film Deposition

Meghnaa Dhanji*, Tuan Nguyen, Steven Luna[1], Zachary Buen[1], Bruno Soriano[1], Julien Manin[1], Lyle Pickett[1]

[1]Combustion Research facility, Sandia National Laboratories

*Corresponding author: lmpicke@sandia.gov

Abstract

Under engine cold-start conditions, Gasoline injections result in fuel deposition on the cylinder surfaces, due to inhibited fuel vapourisation when the contact surfaces are cold, leading to the formation of soot. The Engine Combustion Network's (ECN) Spray G impinging on a wall, under various temperature conditions, was investigated using a suite of optical and surface temperature measurements. The experiments were performed inside a constant-volume chamber under engine-relevant conditions, with sprays impinging on a temperature-controlled wall equipped with nine fast-response thermocouples. The wall was placed 40 mm downstream from the injector to represent typical distance between the piston surface and injector during late injections, a configuration used in cold-starts. Low-Coherence Interferometry was performed for transient fuel film thickness quantification, which provided insights on the film dynamics upon impingement and the evaporation rates. High-speed visualisation techniques further aided in the understanding of transient fuel distribution on the wall. The experimental results were used to validate the Lagrangian-Eulerian simulations of spray wall interactions using the O-rourke and Amsden model with 1-D Conjugate Heat Transfer method. The results captured the dynamic behaviour of the temperature field and film thickness, following initial spray impingement. Differences in the predicted heat transfer was observed due to lack of predictive evaporative cooling of the free spray. Finally, the plume collapse phenomenon was captured by the simulations as the injected fuel was heated.

Keywords

Cold-start, spray-wall interactions, Conjugate heat transfer, film thickness quantification

Introduction

An ongoing challenge associated with GDI engines is achieving a homogeneous charge for the cold-start or part-load operations. One way to optimise the fuel-air mixing and prevent fuel film deposition is to reduce the extent of fuel impingement on the chamber's surfaces. Fuel film formations result in diffusion flame combustion. This is especially common during cold-starts, as the cold surfaces inhibit fuel vaporization.

A handful of experimental studies have focused on the topic of spray-wall interactions. Shway et al. [1] obtained spatio-temporally resolved measurements of film thickness after fuel impingement using UV absorption imaging. The measurements were performed using an 8-hole "Spray G" injector from Engine Combustion Network (ECN) inside a constant volume chamber, with a transparent plate mounted 30 mm from the nozzle exit and perpendicular to the injector axis. The measurements revealed that the evaporation rate was more prominent at the upstream, inward edges of the fuel films, where the film thickness was smaller than that measured downstream at the outer edges of the spray. Of the total fuel injected in the analyzed plume that impinged on the wall 30 mm downstream, 7% of the initial fuel mass was reported to have remained on the plate 30 ms aSOI.

White et al [2] studied the effects of fuel and ambient temperature on the transient fuel film thickness using high-speed spectral Low-Coherence Interferometry (LCI) technique. The main objective was to study the LCI diagnostics to implement it for film thickness quantification used in sprays research. Thicker films were observed with the case where the fuel, wall and chamber temperatures were 20 $^{\circ}$C, when compared to conditions where the fuel, wall and chamber were heated to 90 $^{\circ}$C.

Schulz et al. [3], performed infrared thermography to study the fuel deposits on the walls of a combustion chamber using a heated Nickel alloy plate as substitute to the piston surface. They analysed the heat transfer effects of plume impingement by varying four features: the impact angle of the spray jet, the axial distance between the injector and the heated plate to 15 mm, 25 mm and 50 mm, the wall temperature, and the injection pressure which was set to 5 MPa, 15 MPa and 30 MPa. A decrease in the wall surface temperature at the spray impingement region was measured. A high injection pressure and plume's impact angle adjustment were recommended in order to reduce the mass of film accumulated on the wall. Increasing the injection pressure had raised the heat flux and had resulted in a reduction in the wall film mass. With increasing axial distance between the nozzle and the wall, the wall heat flux had decreased, which was a consequence of the increased impact area.

Efforts in improving simulations to predict fuel film deposition are also on-going. Torelli et al. [4] modified the Stanton and Rutland (SR) model [5][6][7] so as to estimate the impingement frequency for Lagrangian parcels in a Lagrangian-Eulerian (L-E) framework. The original SR model is based on a multi-droplet impingement theory stemming from Yarin and Weiss [8]. They compared the outcomes against experiments and O-Rourke and Amsden (OA) model [9], which is based on correlations against the outcomes from an experiment of a single droplet impingement [10]. One of the major differences between both models was how the amount of splashed mass was determined

with respect to the impinging droplets mass, as well as the rebound velocity. For details on both models, readers can refer to [4]. The authors reported that the pre-impingement Physics and liquid-gas interaction, along with improving splash predictions was key to improving the accuracy of the L-E Computational Fluid Dynamics (CFD) simulations of spray-wall interactions (SWI). Additionally, accounting for surface roughness enabled better predictions of SWI related quantities including spray rebound radii and heights. There was however a mismatch reported in spray height between the CFD and experimental results, which needed to be addressed in the future studies.
Ahamed et al. [11] implemented the drop-wall interaction model in their work. One of the key focuses was to better predict the spray pattern, penetration length and droplet distribution by comparing the outcomes with measurements performed in a constant volume chamber. They reported that the models, including the OA model, under-predicted the spray rebound due to the lack of consideration of the wall roughness, which could determine whether the droplets are more likely to rebound or slide along the wall. They also noted that their 'ARL' model was sensitive to wall temperature. As a result, for the cold-start condition (i.e., wall temperature of 253 K), the model was able to predict more wall film than the standard OA model. However both models lacked validation of the fuel mass and thicknesses from experimental results.
The current campaign aims to address these questions. The effects of fuel impingement on the wall surface temperature and the transient fuel film thicknesses are experimentally and computationally compared and reported. Previous work [12] focused on the effects of fuel, wall and ambient temperature on the extent of surface cooling of the wall upon fuel impingement via experimental diagnostics. The wall was placed 40 mm downstream from the injector tip. Low ambient pressures were employed to mimic injections in the intake stroke. Three key findings from that work were as follows. 1) Wall surface cooling upon fuel impingement was observed for all tested cases - cold condition, hot condition and heated fuel condition where the ambient and wall were cooled. This was due to evaporative cooling of the vaporising free spray as a result of fuel-air entertainment; 2) Plume collapse was observed in the temperature traces with the heated fuel conditions, which led to larger surface area between the plumes being cooled as a result of reduced separation between plumes; 3) LCI measurements showed reduction in mean film thickness over time which was indicative of fuel film vapourisation . The reduction in thickness had stagnated past 40 ms aSoI as preferential evaporation led to the heavier components in PACE20 left deposited on the wall.

Experimental Setup
Fuel was injected into Sandia's optically-accessible constant flow spray vessel. The test injector used was a solenoid actuated, 8-hole ECN "Spray G" injector by Delphi [13]. The injector was designed to offer an 80° spray angle, while the orifice drill angle was 37° relative to the nozzle axis. It is worth noting, however, that the plume direction may not be the same as the drill angle due to the complexities associated with the internal nozzle flow as well as the plume to plume variations.
A 9 component E10 surrogate fuel developed at Sandia National Laboratories, PACE20 was used for the measurements. The components in PACE20 and their liquid volume fractions are listed in Table 1. A double injection strategy was employed, with the electronic injection duration of 0.78 ms for both injections, and a dwell time of 1 ms. The injected mass was 10.3 mg per injection, resulting in a total mass of 20.6 mg. Fuel was injected into the chamber under pure Nitrogen environment.

Table 1. The nine components in PACE20 and their ratios.

Component	Liquid Volume Fraction
Iso-Octane	0.2505
n-Pentane	0.1395
1,2,4 trimethyl benzene	0.1187
n-Heptane	0.1153
CycloPentane	0.1050
Ethanol	0.0955
Toluene	0.0919
1 - Hexene	0.0541
Tetralin	0.0295

Thermocouples and Telemetry System
A temperature controlled wall was placed 40 mm downstream from the injector tip. This position was chosen to be representative of the piston crown location during injection in the intake stroke in a typical GDI engine (310 CAD bTDC for the engine [14]). A liquid circulation pathway 3D printed inside the wall enabled cooled or heated de-ionised water to be circulated around the wall, which controlled the wall's temperature.

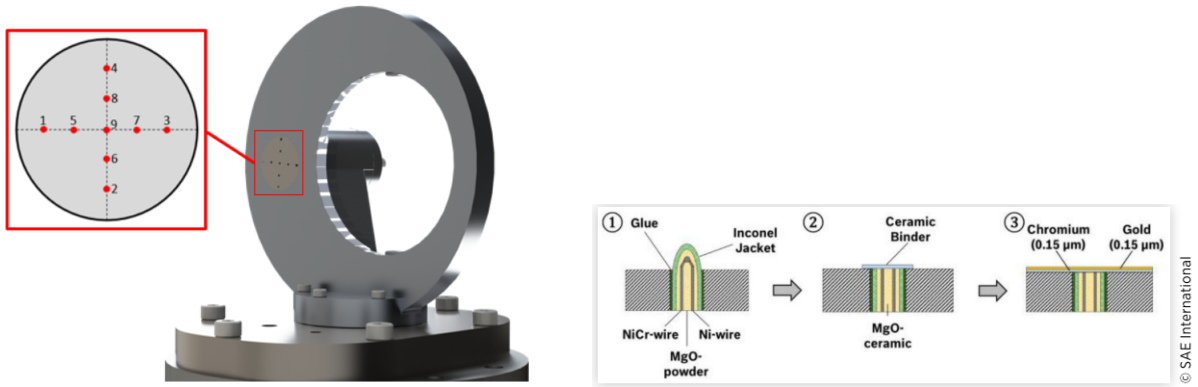

(a) (b)

Figure 1. (a) The temperature controlled wall with the nine thermocouples array mounted and numbered as shown. The wall housed a sapphire window adjacent to the thermocouple probe. This was used for plume thickness quantification using LCI. (b) Detail of thermocouple assembly, image extracted from DOI:10.4271/2018-01-1782 [15].

The thermocouple array was positioned such that one of the 8 plumes was aimed directly towards the array. It housed nine fast-response, thin-surface, K-Type coaxial NiCr-Ni thermocouples, mounted in the orientation shown in Figure 1a. The details of the design were reported by Bargende et al. [15] for a similar thermocouple array. An overview of the way the thermocouples were mounted are shown in 1b.
The thermocouples possess high thermal and mechanical resistance, along with high signal-to-noise ratio and a resolution of 40 µV/K. The high temporal resolution meant that the response time was in the range of a few microseconds. To achieve this, a Cr and Au coating of 0.3 µm was applied. The nine thermocouples were installed inside a housing made of aluminium alloy. The telemetry system consisted of a K-type thermocouple conditioner (AD595), and computer-connected oscilloscope (Picoscope 5000) where the measured voltages were sampled at 100 kHz. To ensure that the thermocouple probe and the corresponding cables were operative under a range of ambient conditions, the probe and the cables were sealed, with the cables housed in an umbilical cord.
The chosen sampling rate and the telemetry configuration resulted in high frequency noise measured along with the temperature trends. In order to attenuate the noise without compromising the detected signal, a Chebyshev Type II filter in Matlab was applied, with a cut-off frequency of 6 kHz.
The injector was mounted on a rotational stage. This enabled the temperature traces of various plume locations to be captured, which was used to generate a coherent map of the effect of these regions impacting the surface temperature at the wall. The injector was rotated at 5° increments from the center position with respect to the thermocouple array. It was rotated up to 30° clockwise and counter clockwise.
The temperature measurements were averaged over 25 injection repetitions for each test case and injector rotation. In order to better interpret the surface temperature variations caused by the impinging fuel, we report the temporal trends of the temperature difference $\Delta T = T_0 - T_i$.

Low Coherence Interferometry (LCI)
The LCI technique was used for film thickness quantification. It works through the use of light travelling through two separate optical paths, one through the region of interest consisting of the test medium (in the case of the current work, fuel film), and one through a known reference point, the fuel-wall interface. The interaction of the two combined light beams reflected from the respective ROIs then produces an interference pattern which has information on the relative path lengths encoded. The interference pattern is then detected by a sensor. For details on the development of the LCI diagnostics technique for film thickness quantification, refer to [2].
In the current work, the detected LCI signal is spectrally resolved and inferred by analysing the interference patterns in the measured spectrum of wavelengths. The Fizeau configuration was employed as it was deemed more effective inside closed chambers for accurate film thickness characterization [2]. In this configuration, the reference light path is produced by the liquid-wall interface due to the differences in the refractive index between the fuel and transparent wall. Using a volume fraction-weighted average gives an estimated index of refraction of 1.4 for the PACE20 fuel. The material thus chosen for the wall was sapphire (5 mm thickness), which has a high index of refraction. The Sapphire wall was held by a custom-designed aluminum retainer with a 50 mm aperture.
A broadband light source (SST-40 N5 6500K broadband LED) illuminated the image and a beam splitter was used to guide the light along two paths and recombine them. The measurements were performed at LED pulse rate and acquisition rate of 10 kHz. The signal was detected with spectral resolution using a high-speed CMOS camera (Photoron SA-Z) coupled to a 320 mm focal length imaging spectrograph (Princeton Instruments Isoplane SCT 320). 150 line/mm grating was used, resulting in 0.0159 nm/pixel resolution. The medium-coarse grating was used to increase the spectral light intensity reaching the sensor to maintain an adequate SNR without compromising the spatial resolution.
A three-piece combination of lenses were used to obtain a conjugate image to be detected by the camera and spectrograph. These were a 200mm f/4.0 lens, a 20× Mitutoyo APO, and a 50mm Nikkor lens, similar to that of

Schumacher et al. [16].
The relatively thin films caused the film thickness signal to exist near the DC component in the scattering potential. To allow for better identification of the film thickness, averaged images were subtracted from each frame prior to computing the Fourier transform. The averages were computed using the 150 frames before and the 150 frames after the frame being observed. Because the interference signal from the film is dynamic, it does not appear in the averaged frame, and so the average subtraction removes most of the DC signal while preserving the thickness information. As an additional step, measured film thickness $\leq 0.45\,\mu m$ was rejected.
A thresholding strategy to identify peaks in LCI scattering potentials and infer the corresponding fuel film thicknesses was adopted in the signal processing. First a root-mean square of the noise floor in the scattering potential was obtained, and a threshold 4 times greater than this noise floor was chosen to detect the signal from the film. Any run of three or more consecutive values above the threshold in a row of the scattering potential was considered a candidate film thickness measurement. Gaussian curve fitting using the Levenburg-Marquardt nonlinear optimization algorithm in MATLAB was applied to those regions. If more than one candidate for film thicnkess was detected, the Gaussian fitting of the region with the maximum number of pixels was used. The film thickness for that spatial location was taken to be the center z value of the fitted Gaussian curve. If no candidates met the threshold in a row, then the measurement was marked as signal dropout. Note that this dropout could be due to the wash- out phenomenon described in the previous section [2] or could be caused by evaporation.
Some of the film thicknesses extracted by this method showed large deviations from the values of many nearby points. Because the spatial and temporal variation of thickness in the film was well-resolved by the LCI system, these sudden deviations and extreme outlier values can safely be labeled as spurious and removed. A median filter with a five point temporal window width was applied to the data at each spatial location to reject errant points and outliers. Additionally, dropout points surrounded on both sides by successful film thickness measurements should have been resolved by the system. To mitigate spurious dropout, points that experienced dropout and were less than three time points away from a successful measurement were filled with linear interpolation from the neighboring successful thickness measurements.

Computational Fluid Dynamics setup
The L-E CFD simulations presented were performed using the CONVERGE software version 3.0. The models and sub-models needed to describe the L-E coupling of the liquid spray with the gaseous phase were either already available in CONVERGE or were implemented in the form of user-defined functions (UDFs). The CFD code has been extensively validated in the past under non-reacting and reacting conditions. LES Dynamic structure was employed to model the turbulence effects in the flow field. The flow field was solved using the PISO algorithm with density based convergence criterion.
The SWI was modeled using the OA model [9]. This model was able to reproduce the washout dynamics as the first fuel impinged on to the surface of the wall and was pushed radially outwards (away from the injector tip), while the second injection impinged onto the deposited film of the wall from the first injection. Less splashing was predicted by the modified SR model (Figure 2) which consisted of the revised droplet impingement frequency formulation compared to the OA model. This led to much higher film deposition and thickness predicted by the OA model.

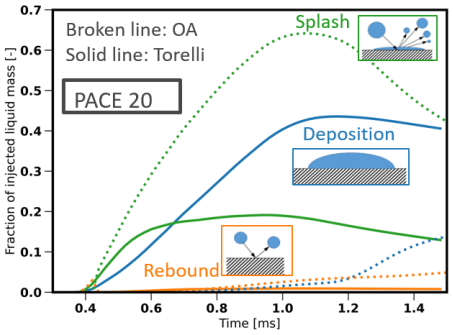

Figure 2. Comparison of splash and film deposition phenomena for OA and modified SR models.

As discussed in the previous section, the OA model is based on correlations obtained from experiments of single droplet impingement. The Weber number of the impinging droplets is a variable threshold, while the non-dimensional splashing parameter is a fixed value. The model assumes a linear splashed mass between two fixed values of the non-dimensional splashing parameter and limits the maximum amount to 75% of the original impinging mass, based on Yarin and Weiss' observations [8]. The velocity of the secondary droplets is modeled using the jet model hypothesis proposed by Naber and Reitz [17].
The liquid spray was modeled using the uniform cone distribution where injected parcels were distributed evenly throughout the cone. The primary liquid atomization of the spray was achieved by means of the BLOB injection model [18]. The secondary breakup on the other hand, was achieved using the Kelvin Helmholtz—Rayleigh Taylor (KH–RT) model as implemented by Patterson and Reitz [19]. The O'Rourke [20] numerical scheme was used to account for droplet collisions and coalescence. Droplet evaporation (i.e. liquid-to-gas phase change) was accounted

through the Frossling correlation and a uniform droplet temperature during thermal transfer was assumed [21]. The coupled momentum exchange between the gas and liquid phases was achieved with the dynamic drag model [22]. The film splashing in spray UDF was used for these simulations.
The setup consisted of 3 boundaries: the chamber wall, the impingement plate and the back of the impingement plate, all of which followed Law of the Wall velocity. The simulations were performed inside a constant volume vessel with an internal volume of 100 cm^3. The wall was located 40 mm away from the injector, normal to the injector axis. The spray cone angle was defined as 32.9°. The injector dimensions were the same as the Spray G injector, with 8 plumes, and the nozzle diameter of 165 µm. Further details of the injector specifications can be found in Table 2.
The wall was 90 mm in diameter and 14 mm thick. 1-D conjugate heat transfer (CHT) mechanism was used to predict the conductive heat transfer on the wall upon the fuel impingement. 9 monitor points along the same position as the 9 thermocouples was added to the wall so as to measure the temperature traces upon the plume impingement. An adiabatic region 10 mm in diameter was applied at the back of the impingement plate to mitigate conductive heat transfer from the impingement region in the opposite side of the wall. The wall was made of Aluminium with a solid layer thickness of 7.6 mm, which mimicked the housing of the thermocouple array to a certain extent.
The minimum mesh size was set to 0.125 mm near the wall and in the near-nozzle region using fixed embedded refinements. Based on the local gradients of velocity, temperature, and gas species, four levels of adaptive mesh refinement (AMR) were used to dynamically achieve the same minimum size of 0.125 mm in those areas where the interaction between the liquid and the gaseous phases occurred. These choices resulted in the peak cell count being 2 million, over the whole simulation time.
The three test cases studied are listed in Table 3. Case 1 represents ECN 'G2 cold condition' [13], representative of injections during cold-start where the fuel and surfaces are cold and the ambient pressure at the beginning of the intake stroke is low. Case 2 represents a condition whereby the injector tip and the fuel are hot (333 K) while the chamber and the wall/piston surface are still cold. Finally case 3 represents a heated engine condition with injection late in the compression stroke where the ambient pressure is atmospheric. The fuel used was PACE20 as defined in the previous section. As such, the 9 components and their liquid volume fraction were specified.

Table 2. Injector specifications and initial conditions

Parameter	Value
Nominal orifice diameter (outlet) (µm)	165
Spray cone angle (°)	32.9
Average discharge coefficient	0.5
Injection pressure (MPa)	20
Ambient gas composition	100%N_2

Table 3. Overview of the test conditions studied. T_{amb}, T_{fuel}, and T_{wall} represent ambient, fuel and wall temperature, respectively. P_{amb} is the ambient chamber pressure.

	T_{amb}[K]	T_{fuel}[K]	T_{wall}[K]	P_{amb}[*bar*]
1	293	293	293	0.5
2	293	333	293	0.5
3	363	363	363	1.0

Results and discussion

The aim was to study the effect of impingement of a single plume of the spray G injector on wall cooling and film thickness. In this case, the plume impingement and film dynamics phenomena of a free spray impinging on a solid surface is schematically presented in Figure 3a. It shows the fuel film formation caused by the plume's head upon impact. This is labelled film center region. As a liquid film settles on the surface, the fuel behind the head of the deflected spray, labelled the 'main wall jet region', propagates parallel to the wall as it faces resistance in its free spray motion from the wall. The wall jet subsequently experiences increasing resistance from the surrounding gases, resulting in the formation of wall jet vortices around the edges of the film center region and the main wall jet region.

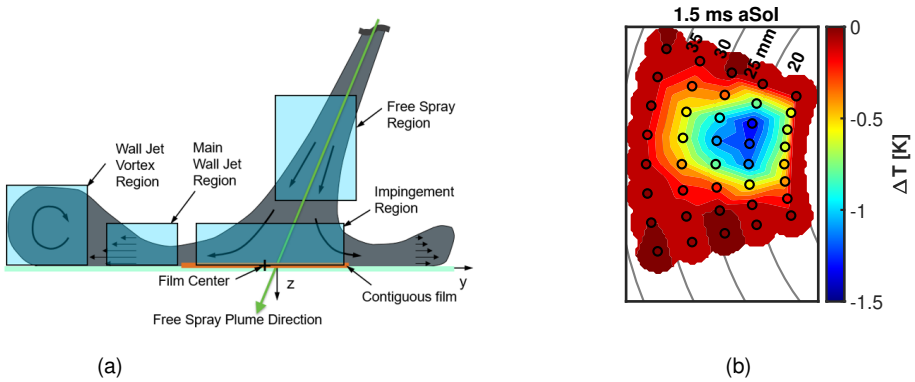

Figure 3. (a) A conceptual model of a single plume impinging on a solid surface. The schematic shows the fuel film center formed upon impingement, while the fuel behind the plume's head moves parallel to the wall in various directions. This generates a wall jet and subsequently a wall jet vortex as it experiences increasing drag caused by the ambient gases (b) Scattered interpolant map of the wall surface temperature at 1.5 ms aSoI for the cold condition (the fuel, wall and chamber at 293 K). The contours represent the differences between the initial surface temperature and the surface temperature at the time of measurement, as represented by ΔT. The distances labelled at the top, 20 to 35 mm, are the radial distances from the injector tip. The back circles show the measurements at injector rotations of 5° increments, while the spaces in between are populated by interpolation.

Effects of fuel impingement on surface cooling

Figure 3b shows the effect of plume impingement on the surface temperature through a scattered interpolant map for the cold condition 1.5 ms aSoI. The contours at each black circles were obtained via injector rotations at 5° increments, while the points in between the circles were obtained through interpolation from the nearby measured data. The labels 20 mm to 35 mm indicate the radial distances from the injector tip. The blue contours or negative ΔT indicates surface cooling upon fuel impingement, while the red contour shows no change from the initial surface temperature.

After the arrival of the plume from the first injection schedule at 1.5 ms aSoI, the surface undergoes cooling. The imprint of the plume regions discussed in Figure 3a is visible in this map: the film center region which forms the most wetted part causes the greatest extent of surface cooling, as observed by the blue contour in the center. The wall jet region can be observed by the lower ΔT surrounding the blue contour.

To understand the reason behind this extent of surface cooling caused by the plume center, we study the predicted mixture temperature for different liquid and vapour mixture fractions via equilibrium-state calculations. The relationship is presented in Figure 4 for Toluene, a heavy surrogate fuel whose boiling point and vapor pressure are similar to that of PACE20. The figure shows the relationship between the adiabatic mixture fraction of the components and their corresponding temperature at the equilibrium state presented in the LHS y-axis. These calculations are performed using standard energy and fugacity balance equations for liquid fuel and gas, which are set to initial set-point temperatures during the experiments. The solid lines represent the adiabatic temperature for a range of mixtures, consisting of liquid and vapourised fuel, and ambient gases. Here, a mixture fraction of unity indicates the liquid exiting the injector, at a temperature of 293 K.

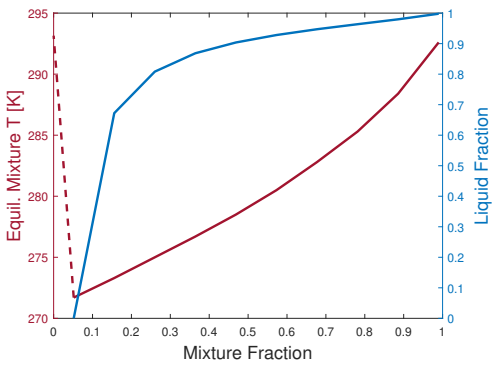

Figure 4. Adiabatic mixture fractions and their equilibrium temperature (LHS axis) and corresponding liquid fraction (RHS axis) for Toluene as a surrogate fuel for PACE20. For the trends associated with the equilibrium mixture temperature, the solid lines represent the mixture containing liquid and vapour fuel mixture, while the dashed lines represent fully vapourised fuel-air mixture. The fuel, wall and chamber temperatures are at 293 K, while ambient pressure is 0.5 bar.

The trend shows that as the mixture fraction reduces with increasing air entrainment, the fuel is undergoing evaporative cooling. Then the dashed lines represent the temperature of the fuel-air mixture that is in the vapour phase under equilibrium state. This line connects the ambient gas temperature (at mixture fraction equal zero) to the

mixture-temperature point where the saturated liquid and vapor envelopes coincide. This point is at a mixture fraction of 0.07, whose equilibrium temperature is 272 K.
The variable profile model of Musculus and Kattke (M-K) [23] helps estimate the radial distribution of the fuel concentration at a given axial distance from the injector. The mixing-limited assumption applied here is that the liquid length is the location on the spray's centerline corresponding to a predicted mixture fraction equal to the saturated liquid-vapor mixture fraction at equilibrium state. A comparison with the experimental studies performed in [24] has shown good agreement between the model and experimental results when using the spreading angles measured with high sensitivity schlieren and matched jet penetration measurements. The model predictions were reported to produce local mixture fractions within the Rayleigh scattering experimental uncertainty.
For the cold fuel, wall and chamber condition, the spray is estimated to arrive at the wall location 0.56 ms aSoI and its mixture fraction here is calculated to be 0.47 using the M-K model. The temperature at this mixture fraction is 280.5 K as per Figure 4, which is lower than the initial wall temperature. When the colder mixture fraction impinges on the surface, the surface is cooled as a result of convective heat transfer away from the wall to the fuel mixture. The RHS y-axis of Figure 4 shows the corresponding liquid fraction at different fuel-air mixture fractions. It is calculated using the following relationship, where Y_L, Y_V and Y_f are liquid, vapour and mixture fractions respectively:

$$Y_L = 1 - \frac{Y_V}{Y_f} \tag{1}$$

At the time of impingement, the liquid fraction of fuel is 0.9, suggesting that very little vapourisation of the fuel in the mixture has taken place. This is why significant cooling is observed around the region impacted by the plume center region which contains mostly unvapourised fuel, or in other words is the most wetted region, under these conditions.
The wall-jet and wall jet vortices are typically made up of low mixture fractions, as high air entrainment has occurred. The mixture fraction is expected to be in the dashed line region in Figure 4, meaning that there is convective heat transfer taking place from the surrounding ambient gases to the mixture. As a result of this, the surface of the wall impacted by the wall jet region undergoes cooling to a lesser extent. This main wall jet region and wall jet vortex are seen in Figure 3b by the yellow and orange contours spreading away from film center region (or the blue contour area).
Figure 5 shows the effects of fuel impingement on the transient temperature reduction for the five separate probe locations. The dotted line shows the experimental results while the solid lines correspond to the computational results. The red envelopes indicate the injection timings of the double injections schedule. The probe numbers with respect to the plume position for both the experiments and simulations are presented in Figure 6.

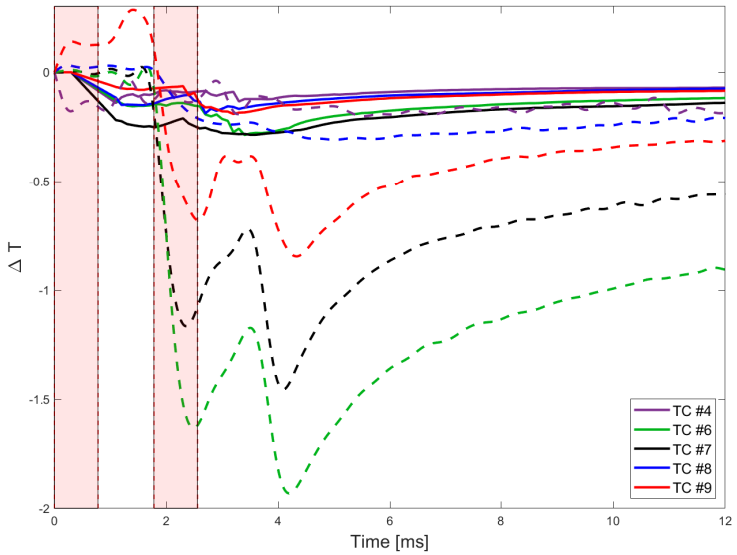

Figure 5. Transient change in temperature after fuel impingement from a double injection strategy measured using five thermocouples in the orientation presented in Figure 6. The solid lines represent CFD results while the broken lines correspond to experimental results. The chamber conditions are: T_{amb} = 293 K, T_{wall} = 293 K, T_{fuel} = 293 K and Pamb = 0.5 bar. The red envelopes represents the double injection timings.

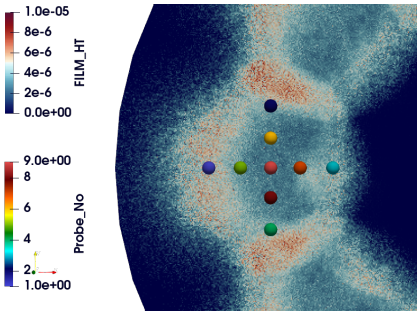

Figure 6. Probes' locations with respect to the film's footprint as simulated at a time instance of 3.1 ms aSoI, so after both injection schedules have occurred.

Comparing the extent of cooling, it is apparent that the simulations are under-predicting the surface cooling when compared to the experiments for all probe locations. In fact, the heavy wetted regions simulated, i.e. probe number 4, shows the least extent of surface cooling.
This can be explained by studying the temperature of the simulated free spray after injection. The temperature of the mixture at four time instances: 0.3 ms, 1 ms, 2.5 ms and 3 ms aSoI are presented in Figure 7. We immediately observe lack of predicted evaporative cooling of the free spray upon injection. In fact, the fuel tends to heat up to a higher value than the initial injection temperature of the fuel. Observing the data at 1 ms aSoI (Figure 7b), the fuel is being cooled upon impingement. This is caused by the cold surface of the wall. As the hot fuel impinges onto the cold wall, conductive heat transfer takes place from the fuel to the wall, causing the fuel film deposited being cooled. This is why we see an initial dip in ΔT upon impingement.
Figure 7c indicates the cold fuel film deposited on the surface prior to the impingement from the second injection schedule, which again is heated. As a result, when the second injection impacts the wall (Figure 7d), the deposited film is pushed radially outwards as more film gets deposited onto the wall. The presence of the pre-cooled fuel film and the further cooling of more liquid mass after the second injection causes the second and greater extent of cooling we observed after the second injection envelope in Figure 5.

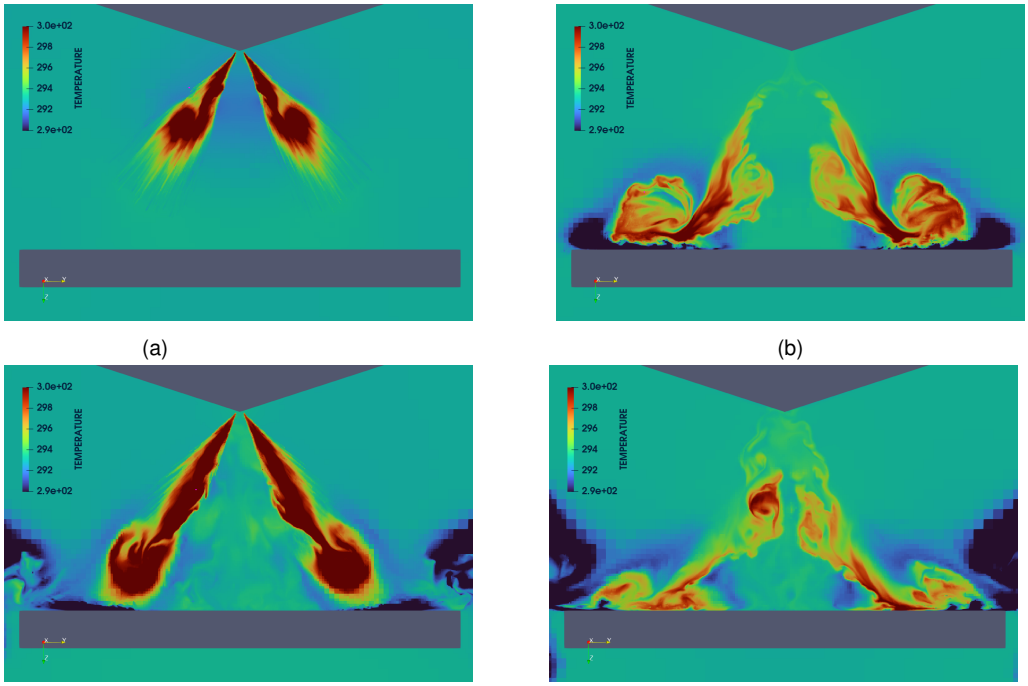

Figure 7. Simulated fuel temperature of the free spray at times (a) 0.3 ms aSoI (b) 1 ms aSoI (c) 2.5 ms aSoI and (d) 3 ms aSoI. The data correspond to the gaseous phase in the Eulerian frame of reference

The predicted mixture fraction of the fuel at the time of impingement, which according to the CFD is 0.56 ms, is approximately 0.47 as seen in Figure 8. The Musculus-Kattke model predicts a mixture fraction of 0.4 at a much earlier impact time of 0.3 ms. The M-K model assumes perfect mixing of air and fuel, but in spite of that, the M-K mixture fraction is comparable to the CFD mixture fraction. Observing the trend in Figure 4, the adiabatic equilibrium temperature at a mixture fraction of 0.47 is equivalent to 278 K. As such, the mixture at the time of impingement

should have been cooled down by 15 K, but instead the simulated temperature reduction is a mere 0.25 K, as observed with probe 7, which is not even experiencing heavy fuel wetting as observed in Figure 6. This is caused by the lack of predictive evaporative cooling, indicating that the SWI model is not able to capture Thermodynamic behavior of the fuel as it changes states.

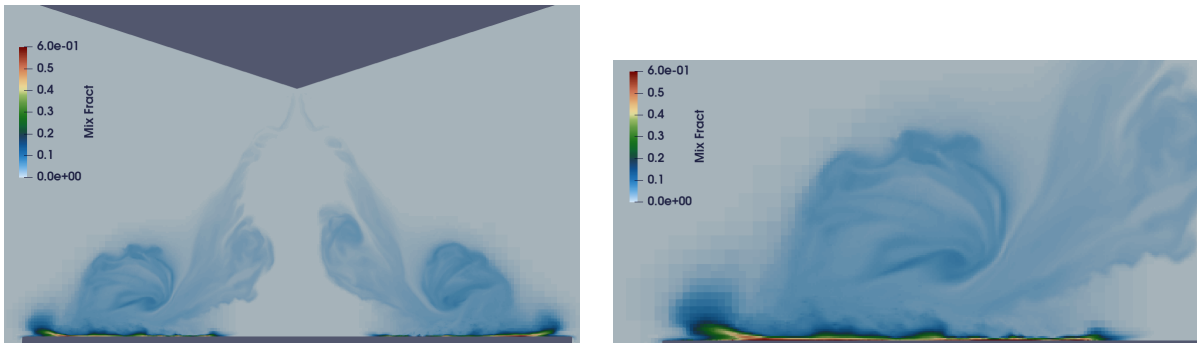

(a) (b)

Figure 8. Simulated mixture fraction of the (a) the global spray at 1 ms aSoI and (b) a close up view of one of the plumes and its mixture fraction.

It is worth noting that there is a delay in the reduction in ΔT between the simulations and experiments. This is mainly because the thermocouples are mounted underneath the 0.3 µs coating. The coating causes the delay in the conductivity to the tip of the probe, hence the delay in the sensitivity of the temperature drop upon the plume's impact, as obserevd i the temperature traces in figure 5.

Film Thickness quantification

This section focuses on the transient mean film thickness trends as measured using LCI, in the efforts to understand the effects of fuel temperature on the evaporation rates of the fuel deposited on the wall. Figure 9 shows the mean film thickness and the dropout rate over time for the experimental case in circles and the numerical simulations presented in stars.

The experimental film thickness presented begin from 15 ms aSoI, which is a long time after the end of both injections. Before this time frame, signal washout was caused from heavy film corrugation, which resulted in 100% dropout rate. This phenomenon is discussed at length in [2]. But to summarise, the LCI signal will disappear or "wash-out" due to the non-unformity in the film thickness caused by insufficient spatial resolution. If the difference in fringe phase changes significantly (by π radians or more) across the projected pixel, then the fringes will cancel out when integrated across the pixel, leading to a loss of signal (wash-out).

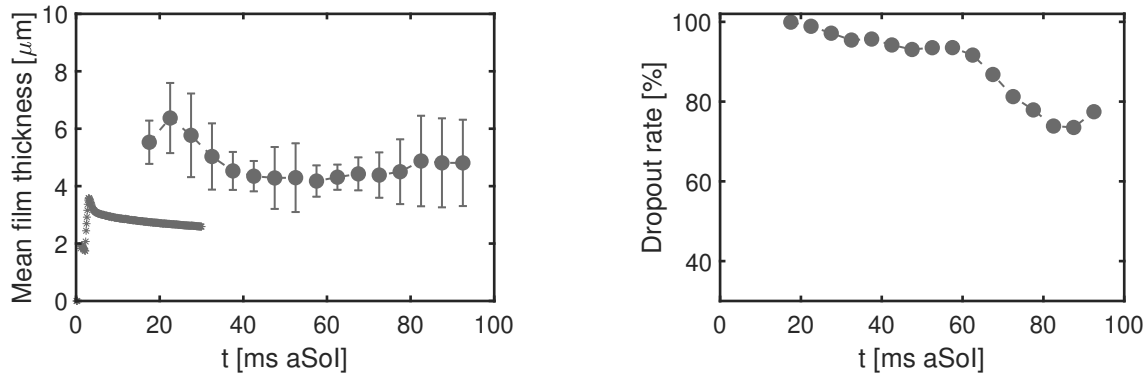

(a) (b)

Figure 9. (a) Comparisons of transient mean film thickness averaged over 25 injections for the experimental results presented in circles and the simulation results presented in stars and (b) transient dropout rate of the LCI signal (experimental).

Observing the experimental film thickness, it initially increases slightly and then reduces until 40 ms aSoI. The reduction in the mean film thickness is indicative of progressive film vapourisation from the wall's surface. After this time, the mean film thickness remains constant with a slight increase over time. This suggests preferential evaporation whereby the lighter components vapourise first, leaving behind the heavier components deposited on the wall for a prolonged time. At this temperature, the vapor pressure of Iso-Octane (highest liquid fraction in PACE20 fuel) is 1734 Pa. In contrast, the heavier component, Toluene, has a vapor pressure of 1166 Pa. Higher

vapor pressure drives faster evaporation, suggesting that the lighter components like Iso-octane vapourise faster. This is why we see a reduction in the mean film thicnkess from 6.8 µm at 20 ms to 4 µm at 60 ms aSoI. Further discussions on preferential evaporation can be found in [12].

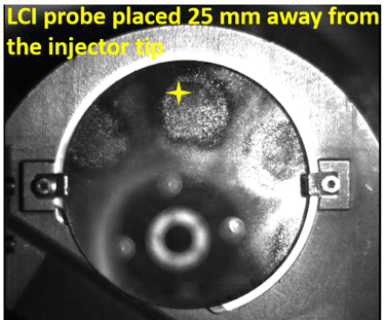

Figure 10. LCI probe location overlaid on top of the plume using high-speed visualisation. The LCI probe is positioned 25 mm from the injector tip, which is visible but out of focus in the image

The difficulty in making comparisons of the film thickness between the experiments and simulations is that the thicknesses have been obtained in two very different ways. The LCI probe location is placed at a radial distance of 25 mm from the injector, whose dimensions are 8 mm by 8 mm. This means that the probe location with respect to the plumes is very small, as shown in Figure 10, and so we are limited in the spatial resolution of the film thickness measurements when considering the global plume structure. The thickness measured using the simulation on the other hand, is obtained by averaging the thickness of the parcels that make up an entire plume. These disparities add complexities to the the way film thicknesses are compared.
As a result, we look at the thickness variation across various plume locations, as presented in Figure 11. The greatest film thickness is around the rim of the plume, which is also seen in the visualisation images in the experiments (Figure 13). The simulated thickness is in the order of 5 µm to 6 µm, 3.1 ms aSoI. The model predicts film deposition around the edges of the plume, which would be the result of liquid film washed outwards from the plume center upon impact. This extent of thickness in the outer edges persists even until 30 ms aSoI, although some film around the rim seems to have evaporated over time.

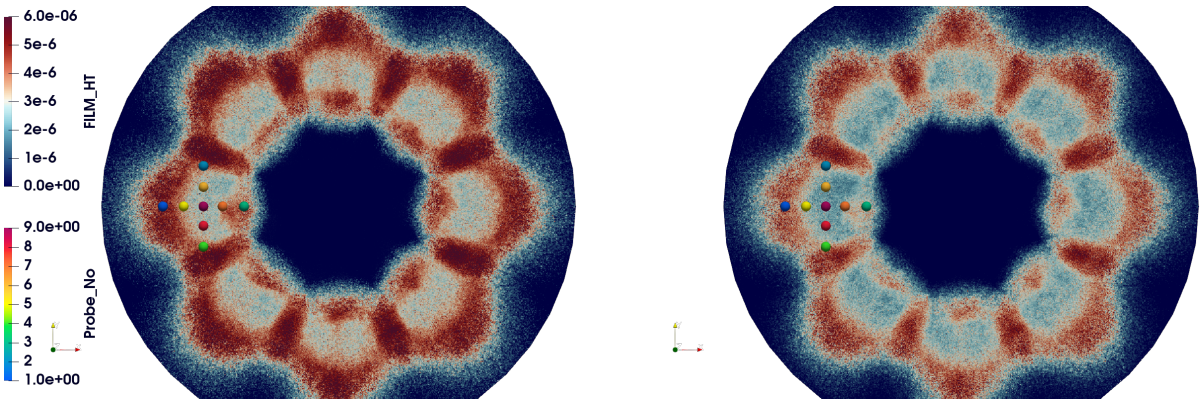

(a) (b)

Figure 11. Simulated film thickness presented at the time instances of (a) 3.1 ms aSoI (b) 30 ms aSoI.

In order to understand the film deposition around the plume, it is useful to understand the liquid distribution just before the spray impacts the wall. Figure 12a presents the liquid volume fraction (LVF) of the free spray obtained from computed tomography (CT) 2 mm above the wall or 38 mm downstream from the injector, while figure 12b shows the simulated LVF at the same distance away from the injector, calculated by dividing liquid parcel volume by the cell volume.
Various differences in the LVF can be observed between the two cases. The simulated results show reduced plume separation compared to the CT data, as a singular ring of liquid volume fraction of the order of 5 mm^3liquid/mm^3volume surrounds the spray for the simulated case. This is where majority of the liquid parcels are distributed across that plane within the free spray. In contrast, the CT data shows distinct separation between each plume and lower LVF around the rims of each plume. The higher LVF associated with the simulated case would cause thick films to form around the rim of the plume upon impact on the wall, as observed in figure 11. The OA model incorporates more splash mass which predicts high film mass and thickness as discussed in a previous section. This trend is also observed in the current results. The higher and more localised LVF around the rim of the plumes, when com-

pared to the experimental data, suggests that the predicted film thickness in these regions would be higher than the experimental case.
In addition, the plumes cover a much larger surface area in comparison to the experimental CT data. This implies that the simulated spray spreading angle and the plume angles are generally much larger compared to the experimental results. Another big contrast is that the peak LVF for each plume is concentrated in the centre of the plume as observed in the CT data, while the computed LVF around the plume center is close to negligible. The liquid parcels' distribution in each plume upstream of the wall affects the spray deposition on the wall. Due to a lack of comparable LVF predicted in the plume centre, even though the liquid spray is modelled using the uniform cone distribution, the predicted thickness at the centre of the plume (figure 11a) is in the order of 2 µm. At this point, it is unclear here as to whether the thickness in the plume centre is also the effect of film washout, in addition to the lack of accurate prediction of the LVF across the plume.

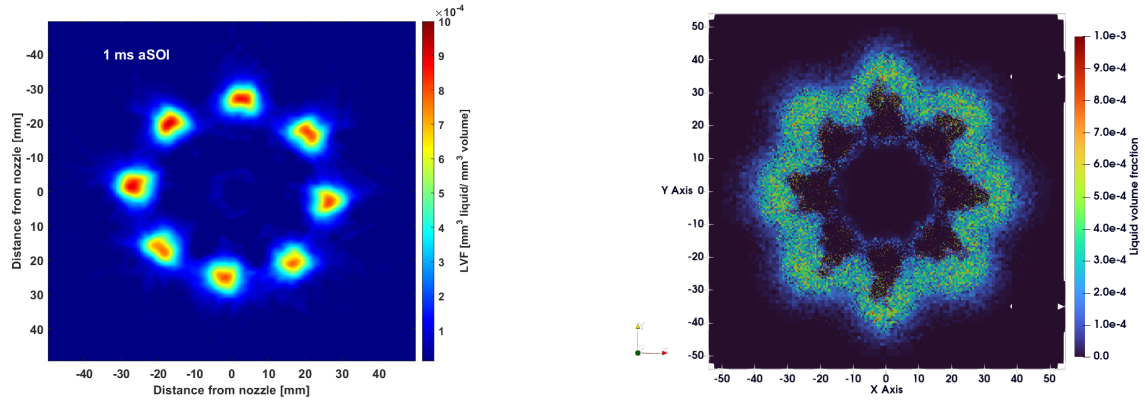

(a) (b)

Figure 12. Liquid volume fraction comparisons for (a) Computed-tomography and (b) simulations at a distance of 38 mm downstream from the injector tip for time stamp 1 ms aSoI.

Effects of fuel temperature on plume collapse

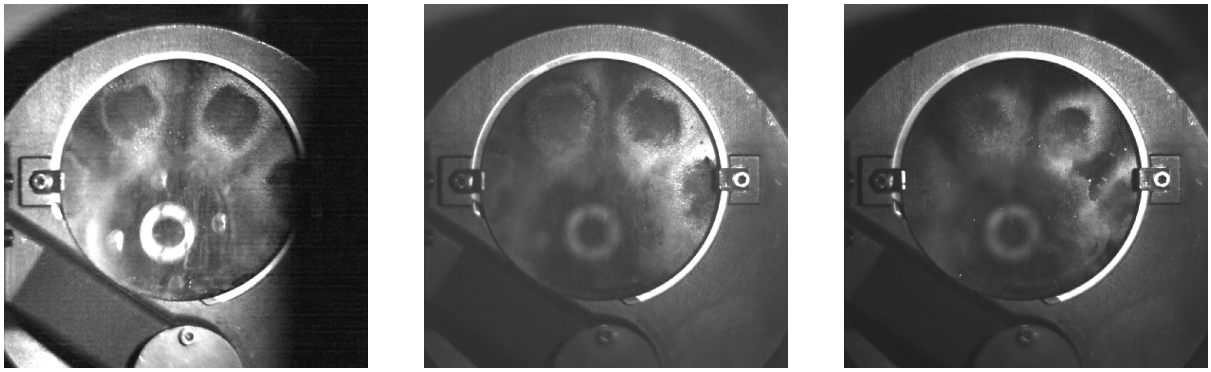

(a) (b) (c)

Figure 13. Plume collapse as evidenced in the high-speed visualisation for conditons: (a) T_{amb} = 293 K, T_{wall} = 293 K, T_{fuel} = 293 K and *P*amb = 0.5 bar; (b) T_{amb} = 293 K, T_{wall} = 293 K, T_{fuel} = 333 K and *P*amb = 0.5 bar and (c) T_{amb} = 363 K, T_{wall} = 363 K, T_{fuel} = 363 K and *P*amb = 1 bar. The time instance is 3.1 ms aSoI, where both injection schedules have arrived at the wall.

As the fuel gets heated, we see evidence of plume collapse, as presented in Figure 13, which highlights the differences in the plume positioning with respect to the injector tip for three different conditions. As the fuel gets heated from 293 K (Figure 13a) to 333 K (Figure 13b), the plumes can be observed to have been edged away from the rim of the fused silica glass piece. In addition, the vicinity of the injector tip seems to be surrounded by a vapour cloud for the heated fuel condition. This phenomenon is more prominent for the condition where fuel is heated to 363 K (Figure 13c). The plumes appear narrower and much further away from the rim of the glass piece, indicating strong plume collapse under this condition.
The plume collapse under heated fuel condition appears to be well captured by the simulations, as presented in Figure 14. While the tail of the plume remains around the same location, near probe 3, the head of the plume gets radially closer to the injector tip. In addition to the plume collapse, the thickness around the rim of the plume is distinctive for the conditions where the fuel temperatures are at 293 K and 333 K, with the ambient and wall

temperature at 293 K (Figure 14a and 14b). The reduced film height in the centre of the plume can also be observed in the high-speed visualisation images (Figure 13a and 13b), which was observed to have been caused by the washout dynamics upon fuel impingement.
This distinction ceases to exist for the hottest fuel condition of 363 K (figure 14c). Instead of showing a variation in thickness, the plume is uniformly thick in all areas beside the tail, indicating that the model is not able to predict realistic film distribution as observed in figure 13c for the heated fuel condition which is approaching flash boiling condition. Note that the ambient pressure under this condition is higher, at 1 bar. Higher ambient pressure encourages greater spray entertainment. As a result, the plume would be expected to be wider with ineven distribution in film thickness. These features are not captured by the simulations as observed.

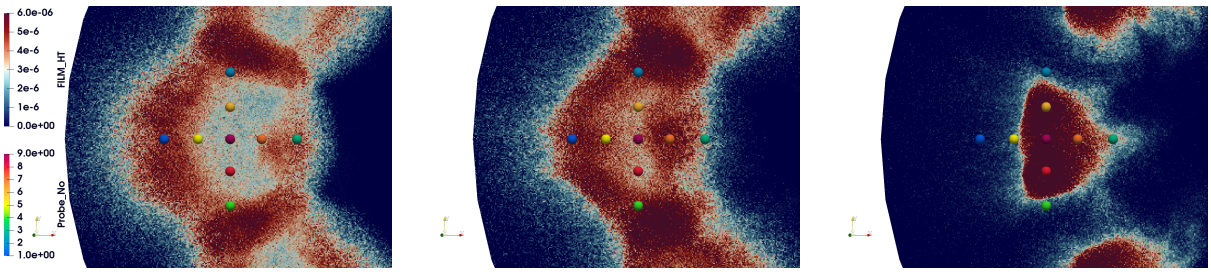

(a) (b) (c)

Figure 14. Simulated plume impingement locations wrt. the probe positions for conditions: (a) T_{amb} = 293 K, T_{wall} = 293 K, T_{fuel} = 293 K and Pamb = 0.5 bar; (b) T_{amb} = 293 K, T_{wall} = 293 K, T_{fuel} = 333 K and Pamb = 0.5 bar and (c) T_{amb} = 363 K, T_{wall} = 363 K, T_{fuel} = 363 K and Pamb = 1 bar. The time instance is 3.1 ms aSoI, where both injection schedules have arrived at the wall.

Conclusions

The spray-wall interactions and their effects on the surface temperature and film thickness were experimentally and numerically evaluated in a constant flow spray vessel. ECN Spray G was investigated at 20 MPa injection pressure under a double injection schedule. A heavy nine-component Gasoline surrogate fuel known as PACE20 was used. The O-Rourke and Amsden model based on single droplet impingement theory and variable splash mass fraction was used for the SWI model as it provided closest representation of the wash-out dynamics of the fuel upon impingement as captured via a series of experimental diagnostics.
The key findings of the work are summarised below.

- Under cold wall, fuel and ambient conditions (293 K), the simulations under-predicted cooling significantly. This was caused by the free-spray heating up to a higher value than the initial injection temperature of the fuel. The lack of predictive evaporative cooling indicated that the simulations were not able to capture Thermodynamic behavior of the fuel/free spray as it changed states.

- Comparisons of the liquid volume fraction between the experiments and simulations revealed the inaccuracy in the simulated LVF of the free spray just before its impact on the wall. The LVF was heavily over-predicted around the rim of the plumes. The centre of the plume, which should show peak in LVF as per the CT data, showed negligible distribution of the LVF. These features would cause inaccurate film deposition upon impingement, potentially leading to higher predicted film thicknesses. In addition, there was a lack of plume separation observed for the simulated case, indicating higher simulated spray angles compared to the experiments.

- Plume collapse was captured by the simulations as the fuel was heated from 293 K to 333 K. In spite of the plume collapse, the simulated plume footprint maintained the differences in the film thicknesses between the center of the plume and rim of the plume which was thicker. While further plume collapse was noted as the fuel temperature was heated to 363 K, a uniformly thick film was observed for this condition, which was not physical given the ambient pressure was also raised to 1 bar.

Acknowledgements

The authors would like to thank Rafael Clemente Mallade and Aaron Czeszynski for their contributions to this work. Sandia National Laboratories is a multi-mission laboratory managed and operated by National Technology and Engineering Solutions of Sandia, LLC., a wholly owned subsidiary of Honeywell International, Inc., for the U.S. Department of Energy's National Nuclear Security Administration under contract DE-NA0003525. This paper describes objective technical results and analysis. Any subjective views or opinions that might be expressed in the paper do not necessarily represent the views of the U.S. Department of Energy or the United States Government.

References

[1] Shway, K., Bardi, M., Bruneaux, G., Kaiser, Sebastian A, 2021, "Quantitative UV-absorption imaging of liquid fuel films and their evaporation". *ICLASS 2021, 15th Triennial International Conference on Liquid Atomization and Spray Systems, Edinburgh, UK, 29 Aug. - 2 Sept. 2021*, 26 (9), pp. 889-919.

[2] White, L., Manin, J., Pickett, L., 2022, "High-speed low-coherence interferometry for film thickness measurements in impinging gasoline direct injection sprays". *The Proceedings of the International symposium on diagnostics and modeling of combustion in internal combustion engines*, doi.10.1299/jmsesdm.2022.10.C3-3.

[3] Schulz, F., Schmidt, J., Kufferath, A., Samenfink, W, 2014, "Gasoline Wall Films and Spray/Wall Interaction Analyzed by Infrared Thermography". *SAE International Journal of Engines*, doi.10.4271/2014-01-1446.

[4] Torelli, R., Scarcelli, R., Som, S., Zhu, X., Lee, S., Naber, J., Markt, D., Raessi, M., 2020, "Toward predictive and computationally affordable Lagrangian–Eulerian modeling of spray–wall interaction", *International Journal of Engine Research*, 21 (2), pp. 263-280.

[5] Stanton, D W., Rutland, C J., 1996, "Modeling fuel film formation and wall interaction in diesel engines", *SAE transactions*, pp. 808 - 824.

[6] Stanton, D W., Rutland, C J., 1998, "Multi-dimensional modeling of heat and mass transfer of fuel films resulting from impinging sprays", *SAE transactions*, pp. 44 - 59.

[7] Stanton, D W., Rutland, C J., 1998, "Multi-dimensional modeling of thin liquid films and spray-wall interactions resulting from impinging sprays", *SAE transactions*, 41 (20), pp. 3037 - 3054.

[8] Yarin, A. L., Weiss, D. A., 1995, "Impact of drops on solid surfaces: self-similar capillary waves, and splashing as a new type of kinematic discontinuity", *Journal of fluid mechanics*, 283, pp. 141 - 173.

[9] O'Rourke, P. J., Amsden, AA., 2000, "A spray/wall interaction submodel for the KIVA-3 wall film model", *SAE transactions*, pp. 281 - 298.

[10] Mundo, C., Sommerfeld, M., Tropea, C., 1995, "Droplet-wall collisions: experimental studies of the deformation and breakup process", *SAE transactions*, 21 (2), pp 151 - 173.

[11] Ahamed, S. Cho, Y, Kong, S.-C., 2022, "Implementation of a Drop-wall Interaction Model Considering High Ambient Pressure for Engine Simulations". *ILASS-Americas 32nd Annual Conference on Liquid Atomization and Spray Systems*.

[12] Dhanji, M., Buen, Z., White, L., Manin, J., Pickett, L., 2023, "A Study of Impinging Spray G on Transient Thermal Loading and Fuel Film Deposition". *ILASS-Americas 33rd Annual Conference on Liquid Atomization and Spray Systems, May, 2023*.

[13] Engine Combustion network, https://ecn.sandia.gov/.

[14] Kim, N., Vuilleumier, D., He, X., Sjöberg, M., 2021, "Ability of Particulate Matter Index to describe sooting tendency of various gasoline formulations in a stratified-charge spark-ignition engine", *Proceedings of the Combustion Institute*, 38 (4), pp. 1540 - 7489.

[15] Mayer, D., Seelig, A., Kunz, T., Kopple, F., Mansbart, M, Bargende, M., 2018, "Experimental Investigation of Flame-Wall-Impingement and Near-Wall Combustion on the Piston Temperature of a Diesel Engine Using Instantaneous Surface Temperature Measurements", *SAE Technical Papers 2018-01-1782*, pp 1 - 18, doi. 10.4271/2018-01-1782.

[16] Schumacher, L., Seel, K., Reddemann, M. A., Kneer, R., 2018, "High-speed Fizeau interferometry for film topography measurement during spray film interaction", *Review of Scientific Instruments*, 89 (11), doi. 10.1063/1.5053591.

[17] Naber, JD., Reitz, RD., 1988, "Modeling engine spray/wall impingement", *SAE technical paper 880107*.

[18] Reitz, RD., 1987, "Modeling atomization processes in high-pressure vaporizing sprays", *Atomis Spray Technol 1987*, 3(4), 309–337.

[19] Patterson, M., Teitz, RD., 1998, "Modeling the effects of fuel spray characteristics on diesel engine combustion and emission", *SAE technical paper 980131*.

[20] O'Rourke, PJ., 1981, "Collective drop effects on vaporizing liquid sprays", *PhD Thesis, Princeton University, Princeton, NJ*.

[21] Amsden, AA., O-Rourke, PJ., Butler, T., 1989, "KIVA-II: a com- puter program for chemically reactive flows with sprays", *Los Alamos, NM: Los Alamos National Laboratory*.

[22] Liu AB., Mather D., Reitz RD., 1993, "Modeling the effects of drop drag and breakup on fuel sprays", *SAE technical paper 930072*.

[23] Musculus, Mark P.B., Kattke, K., 2009, "Entrainment Waves in Diesel Jets", *SAE Int. J. Engines 2(1)*, pp 1170 - 1193, doi.10.4271/2009-01-1355.

[24] Pickett, L M., Manin, J., Genzale, C L., Siebers, D. L., Musculus, M. P.B., Idicheria, C. A., 2011, "Relationship Between Diesel Fuel Spray Vapor Penetration/Dispersion and Local Fuel Mixture Fraction", *SAE International Journal of Engines*, 4 (1), pp 764 - 799, doi.10.4271/2009-01-1355.